

Introduction

- Long-standing debate around whether active regions are heated steadily or impulsively
- Fundamental question: what is the frequency at which individual loops in active regions are reenergized?
- Observations often interpreted in context of nanoflare heating [e.g. 4, 9], though steady heating also possible [16]
- Two primary questions: 1. How do observable signatures vary with heating frequency? and 2. Can we use synthetic observables together with real data to constrain properties of the heating?
- Timelags between AIA channel pairs [13, 14] provide a powerful diagnostic for cooling patterns
- Explore a range of heating frequencies and systematically assess model viability based on detailed comparisons to data—a successful model must be consistent with all observables
- Forward model active region emission using ensemble of field-aligned hydrodynamic models and detailed atomic physics

Pipeline for Forward Modeling Emission from Active Region Cores

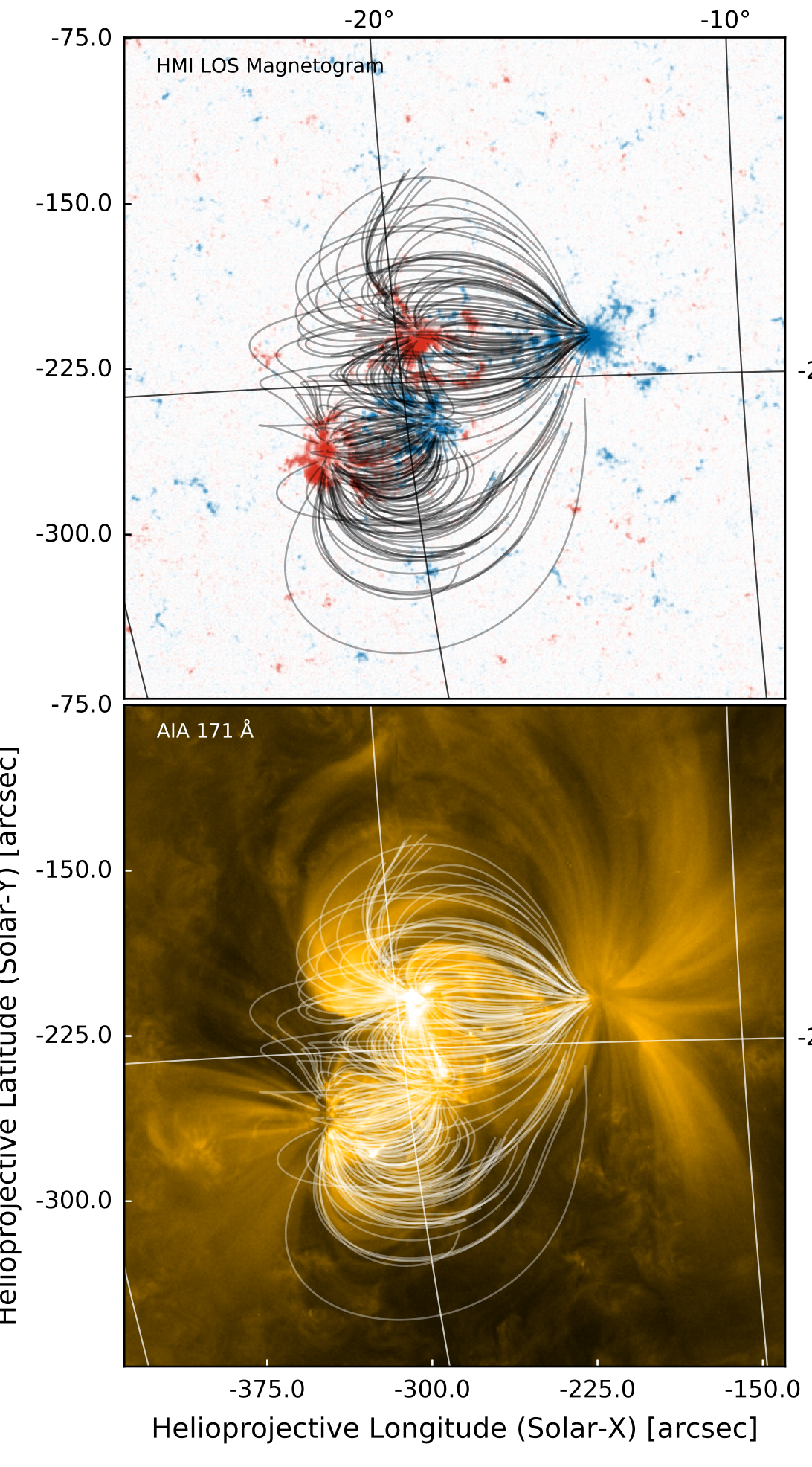


Figure 1: HMI LOS magnetogram (Top) and AIA 171 Å image (Bottom) of NOAA 1158 observed on 12 February 2011 with ~ 250 fieldlines overlaid from a potential field extrapolation

- Select magnetogram for the desired active region. Fig. 1 shows NOAA 1158 as observed by HMI and AIA.
- Perform a field extrapolation to derive the three-dimensional vector field \vec{B} using oblique Schmidt method [12]
- Trace 5000 fieldlines through extrapolated field, including only closed fieldlines with loop lengths in the range $20 < L < 300$ Mm.
- For each fieldline, run a field-aligned hydrodynamic model. In this case, we'll use the two-fluid ebtel++ model described in Barnes et al. [1] and compute 3×10^4 s of evolution
- Using T_e and n_e from hydrodynamic model, calculate emissivity for each selected transition λ_{ij} of element X and charge state k,

$$P_{ij}(X, k) = \frac{n_h}{n_e} Ab(X) f_{X,k}(T_e) N_j(n_e, T_e) A_{ij} \Delta E_{ij} n_e$$

- $Ab(X)$, N_j , A_{ij} , ΔE_{ij} all computed or read from CHIANTI v8.0.6 [18, 6]
- Coronal abundances from Feldman et al. [7]
- Include all transitions of all ions from calcium, iron, magnesium, nickel, oxygen, silicon, and sulfur
- $f_{X,k}$ calculation includes effects due to nonequilibrium ionization using methods of [2]
- T_e , n_e functions of h , the distance along the LOS which intersects many loops

- Integrate the emissivity along the LOS for each transition and convolve with the instrument response,

$$I_c = \frac{1}{4\pi} \int_{\text{LOS}} dh \left(\sum_{\{ij\}} P_{ij} R_c(\lambda_{ij}) \right)$$

where R_c is the AIA wavelength response for channel c and I_c is the resulting channel intensity

- Convolve with the point spread function of the instrument.

Heating Model: Impulsive Heating over a Range of Frequencies

- Parameterize heating in terms of discrete triangular pulses of duration 200 s occurring on individual strands, i.e. nanoflares [10]
 - Define the heating frequency in terms of the loop cooling time τ_{cool} such that,
- $$\varepsilon = \frac{\langle t_{wait} \rangle}{\tau_{cool}} \begin{cases} < 1, & \text{high frequency,} \\ \sim 1, & \text{intermediate frequency,} \\ > 1, & \text{low frequency} \end{cases}$$
- where t_{wait} is the time between successive events on a given strand
- Choose event energy E_i from power-law distribution $P(E_i) \propto (\epsilon B)^2 / 8\pi$, $\alpha = -2.5$
 - Waiting time prior to each event chosen such that $t_{wait} \propto E_i$ following model of Cargill [5]—the longer the field is stressed, the greater the energy release
 - Constrain the total flux into the AR to be $\approx 10^7$ erg cm $^{-2}$ s $^{-1}$ according to observations by Withbroe & Noyes [17]
 - Include two additional control models:
 - "Cooling"—Each strand heated by single pulse at $t = 0$ s with energy $(\epsilon B)^2 / 8\pi$
 - "Random"—Each strand heated by single pulse at some random time in $0 < t < 3 \times 10^4$ s with energy $(\epsilon B)^2 / 8\pi$

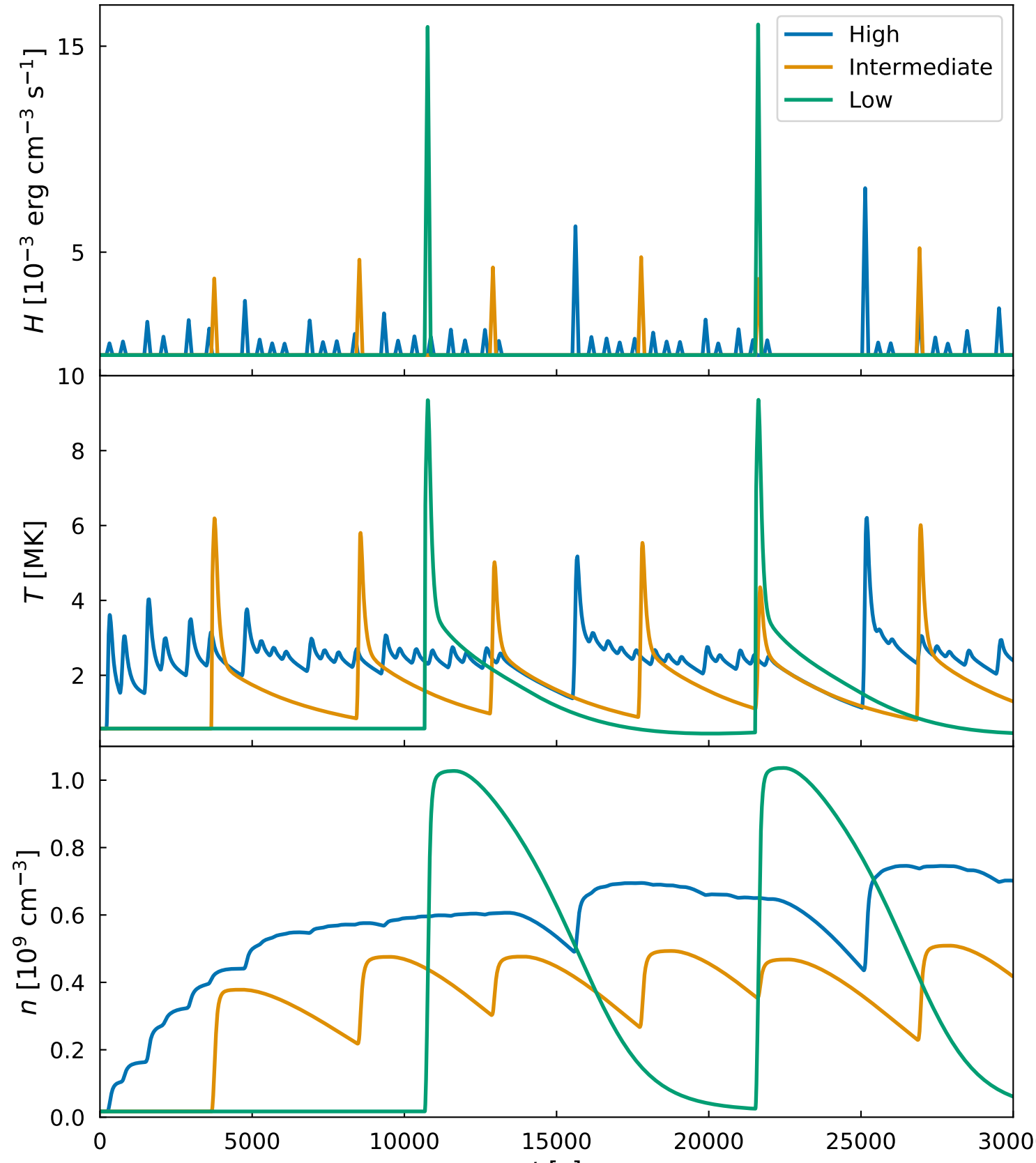


Figure 2: Heating profile (Top), electron temperature (Middle), and density (Bottom) for each heating frequency for a single loop in the active region.

Simulated AIA Intensities

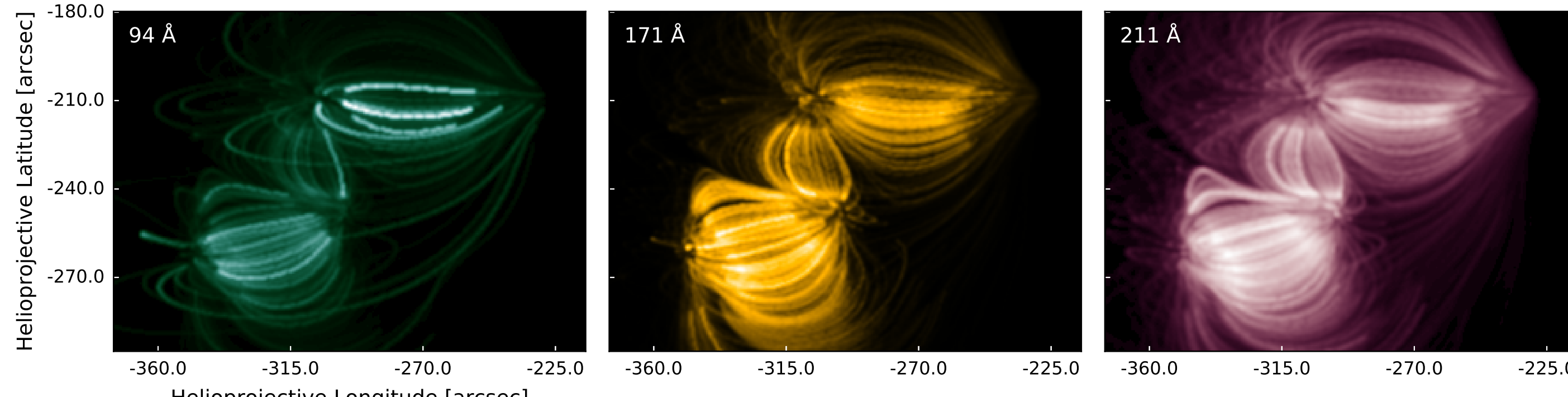


Figure 3: Snapshot of intensity at $t = 2.5 \times 10^4$ s in three AIA channels for the intermediate frequency case

Computing Timelags Between AIA Channel Pairs

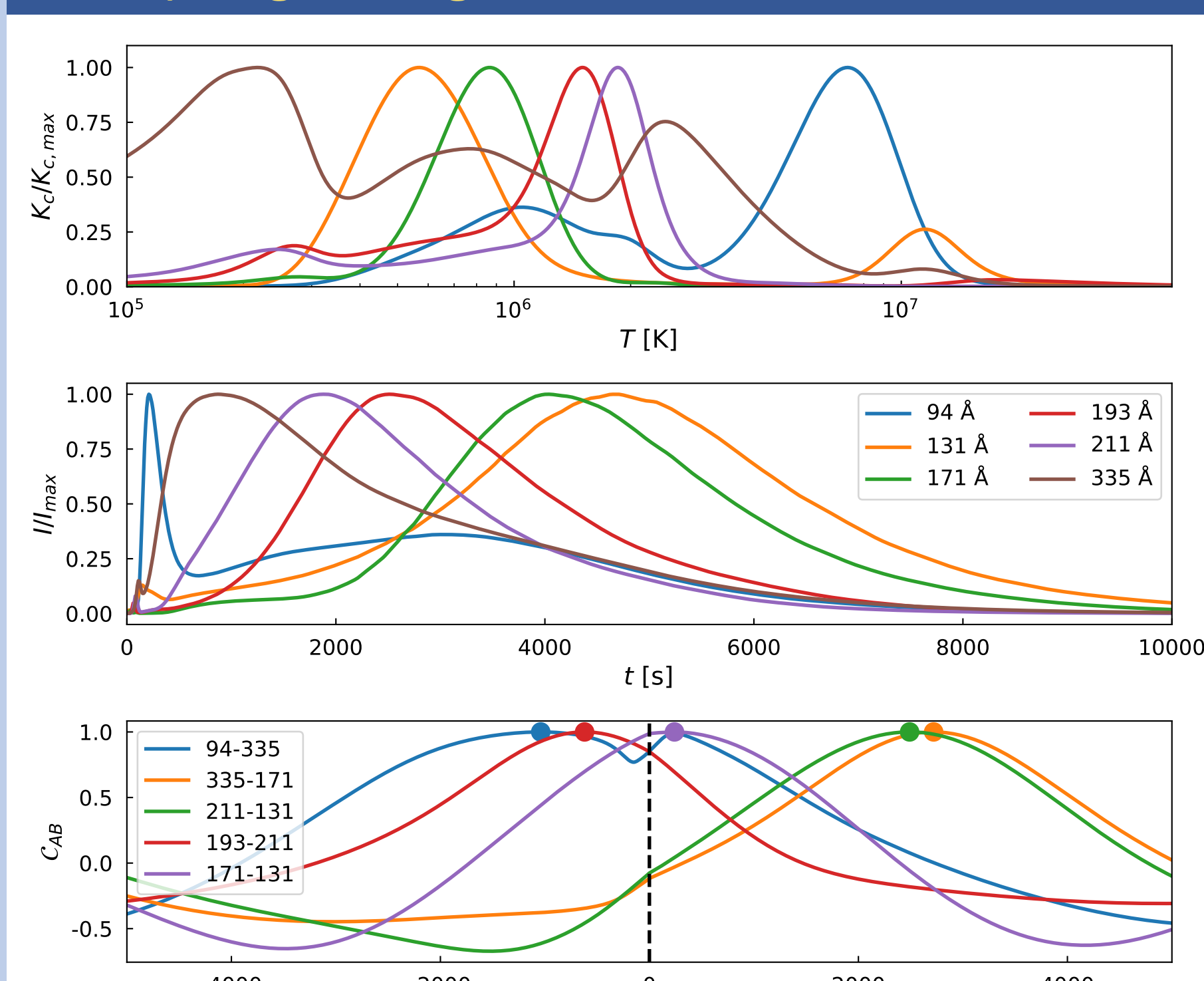


Figure 4: Top: AIA temperature response functions for 6 EUV channels; Middle: Normalized pixel-averaged AIA intensity for the "cooling" case described above; Bottom: Cross-correlation curves for selected channel pairs

- As coronal plasma cools, the intensity peaks in successively cooler AIA passbands (see top panel of Fig. 1)

- Understand relationship between these peaks by computing cross-correlation between channel pairs
- The cross-correlation between two channels A and B as a function of the offset τ can be expressed as,

$$\begin{aligned} C_{AB}(\tau) &= I_A(t) * I_B(t) = I_A(-t) * I_B(t), \\ \mathcal{F}\{C_{AB}(\tau)\} &= \mathcal{F}\{I_A(-t)\} * \mathcal{F}\{I_B(t)\} \\ &= \mathcal{F}\{I_A(-t)\} \mathcal{F}\{I_B(t)\} \end{aligned}$$

- Define the timelag τ_{AB} as that offset which maximizes the cross-correlation,

$$\tau_{AB} = \arg \max_{\tau} (C_{AB}(\tau))$$

- By convention, order hot channel first such that positive timelags indicate cooling plasma
- Compute τ_{AB} in each pixel between -6 hours and +6 hours from 2×10^4 s of simulation time

Simulated versus Observed Timelags

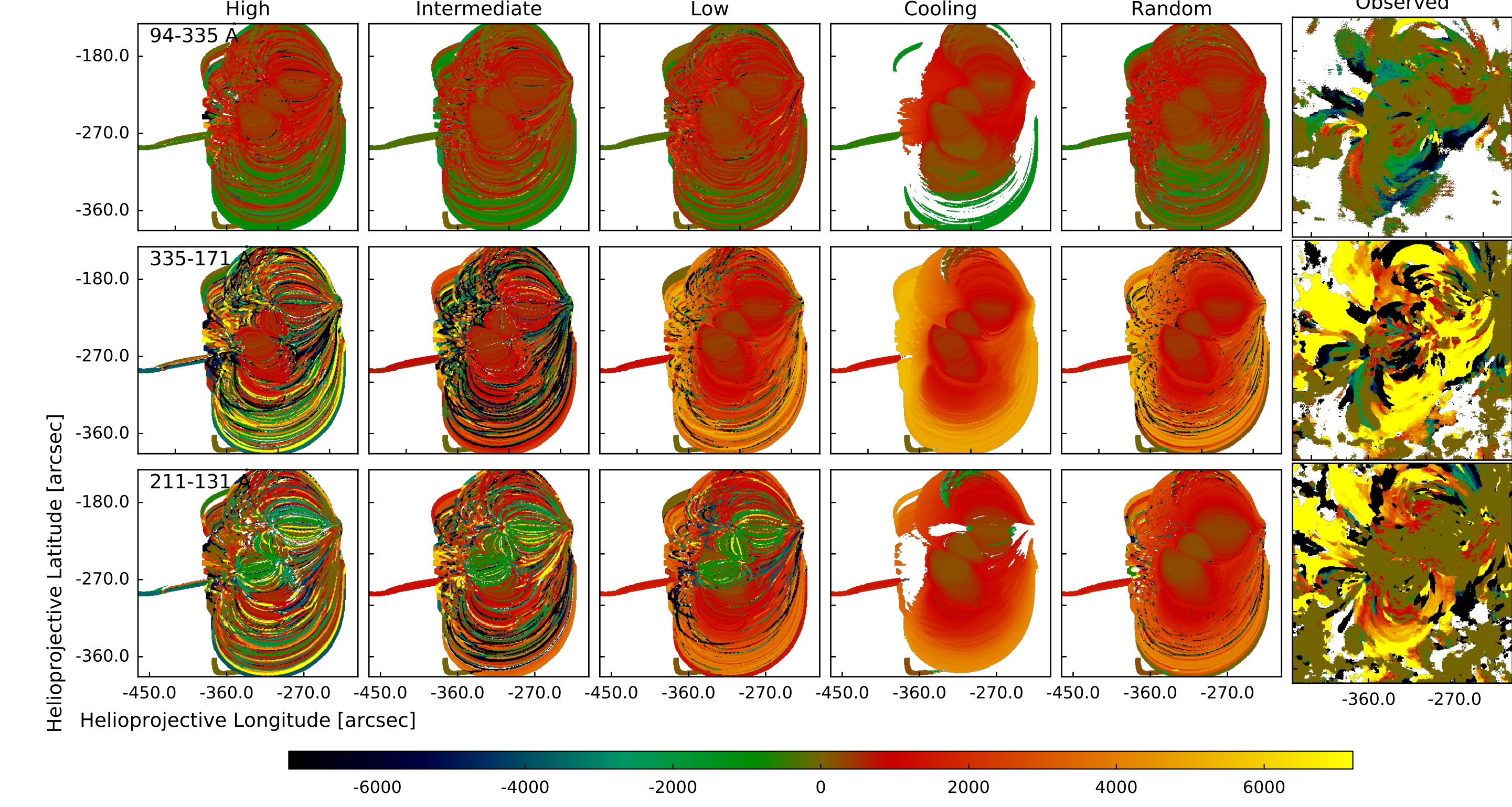


Figure 5: τ_{AB} computed in each pixel of the AR for all five heating cases and observed intensity for three selected channel pairs. Note in particular the presence of negative timelags in the 131 Å pair for the low, intermediate, and high frequency models and their absence in the observation

Analyzing Observed Pixels with a Random Forest Classifier

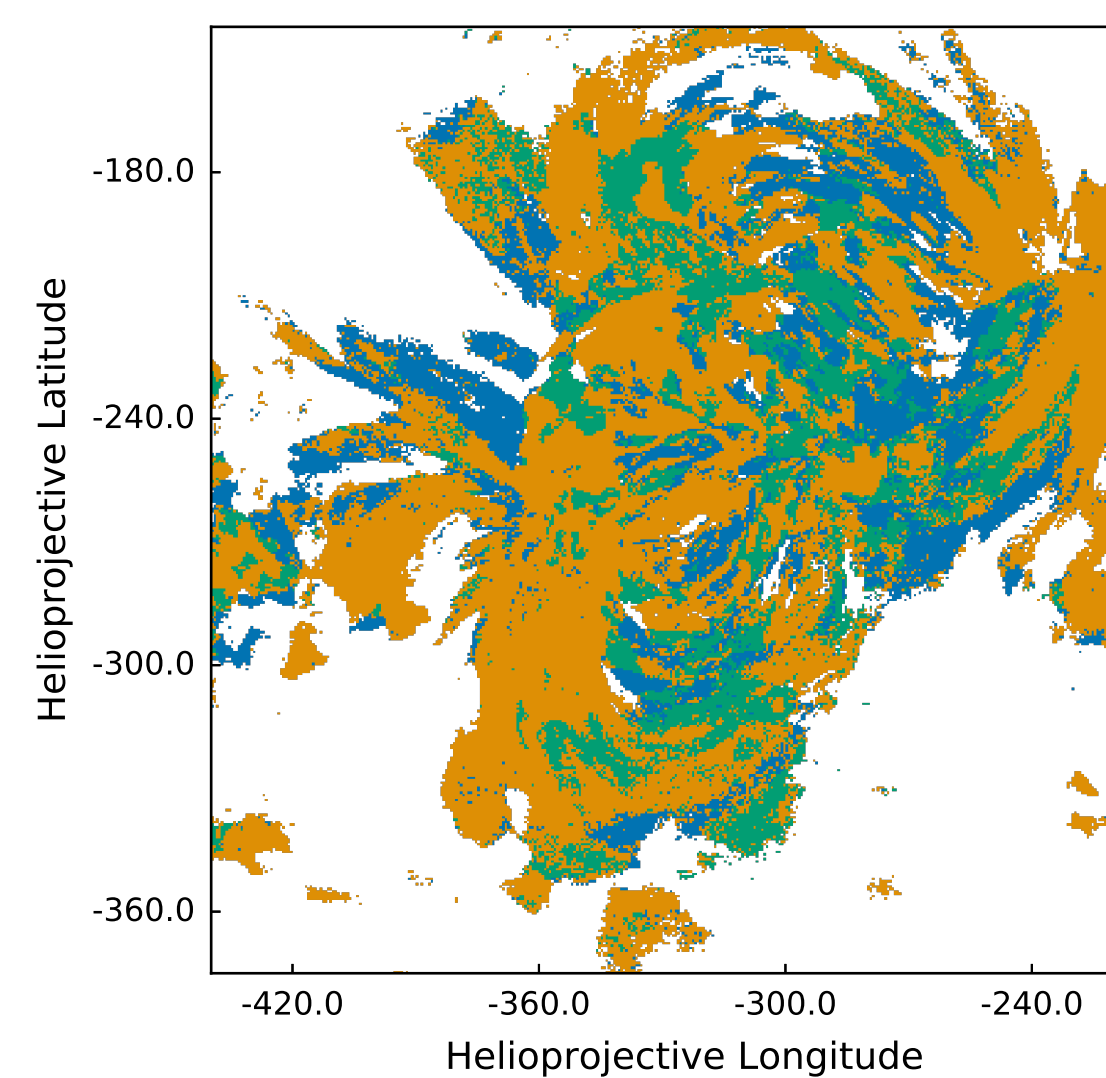


Figure 6: Top: Discrete classification of each observed pixel according to the random forest classifier. Bottom: Class probability of each heating model. The classification of each pixel is determined by the most probable class (i.e. heating model)

Comparing to Emission Measure Slopes

- Compute emission measure distribution $\text{EM}(T)$ from time-averaged AIA intensities in each pixel using method of Hannah & Kontar [8]
- Calculate power law index a such that $\text{EM} \sim T^a$ between 1 and 4 MK
- Shallower slope indicates broad distribution of temperatures and thus lower frequency (and vice versa) [see 3, 15, and references therein]
- Observed range of slopes is broad, indicating a range of heating frequencies over the active region core

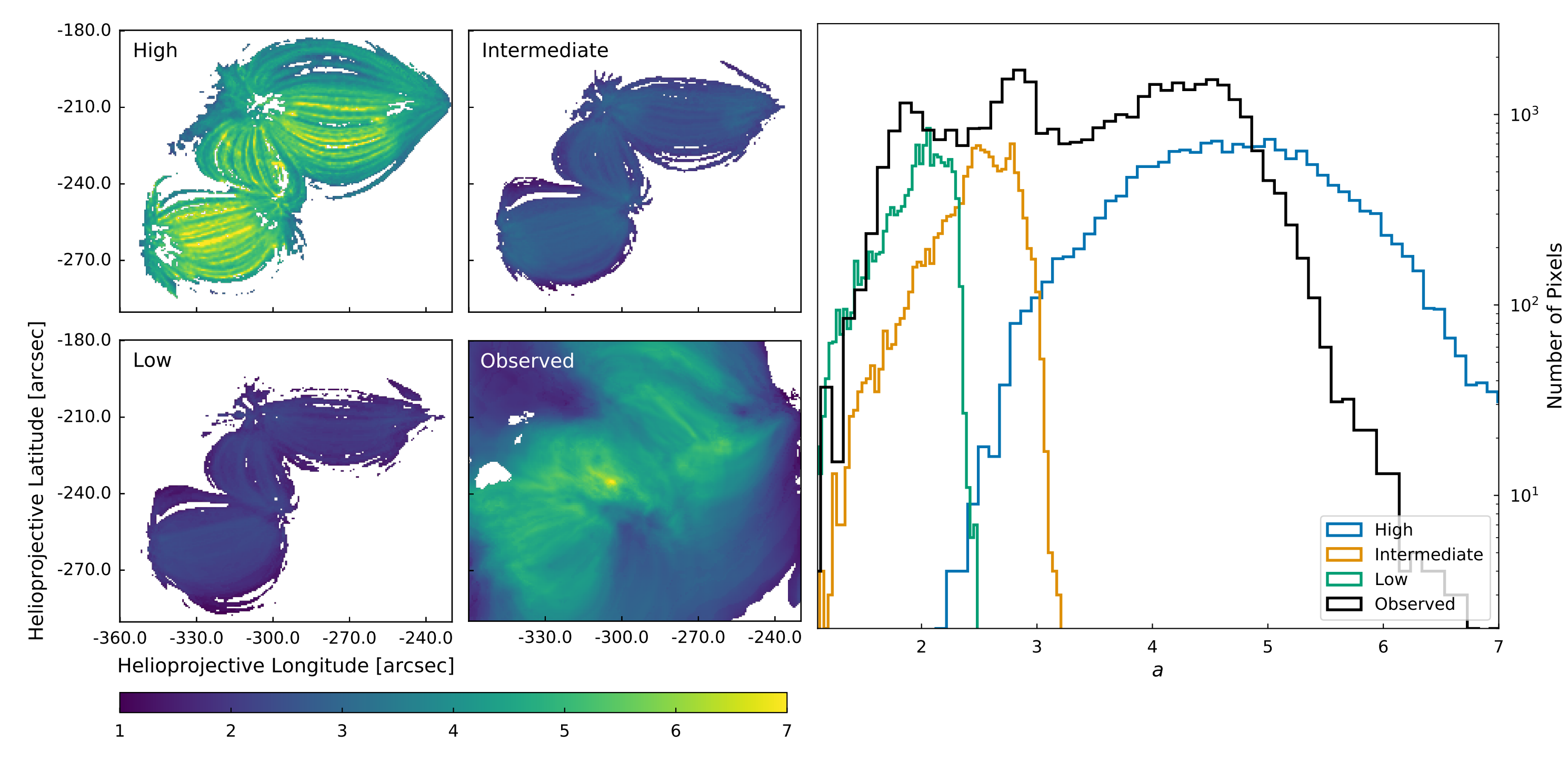


Figure 7: Left: Emission measure slopes derived from model intensities for three primary heating models and observed intensities. Right: Distribution of emission measure slopes over the active region core.

Conclusions

- Developed flexible, extensible pure Python pipeline for efficiently modeling coronal emission
- Computed timelags suggest core emission < 10 MK and heated at sufficiently high frequency, longer loops on periphery heated at lower frequencies
- Application of random forest classifier suggests dominance of intermediate frequencies over whole AR
- Emission measure slopes show need for range of heating frequencies across the AR core
- Combination of forward modeling, multiple observables, and classifier approach provide a powerful method for systematically assessing heating model viability

References

- Barnes, W. T., Cargill, P. J., & Bradshaw, S. J. 2016, *The Astrophysical Journal*, 829, 31
- Bradshaw, S. J. 2009, *Astronomy and Astrophysics*, 502, 409
- Bradshaw, S. J., Klimchuk, J. A., & Reep, J. W. 2012, *The Astrophysical Journal*, 758, 53
- Brosius, J. W., Daw, A. N., & Rabin, D. M. 2014, *ApJ*, 790, 112
- Cargill, P. J. 2014, *The Astrophysical Journal*, 784, 49
- Dere, K. P., Landi, E., Mason, H. E., Fossi, B. C. M., & Young, P. R. 1997, *Astronomy and Astrophysics Supplement Series*, 125, 25
- Feldman, U., Mandelbaum, P., Seely, J. F., Doschek, G. A., & Gursky, H. 1992, *The Astrophysical Journal Supplement Series*, 81, 387
- Hannah, I. G., & Kontar, E. P. 2012, *Astronomy and Astrophysics*, 539, A146
- Ishikawa, S.-n., Glesener, L., Krucker, S., et al. 2017, *Nature Astronomy*, 1
- Parker, E. N. 1988, *The Astrophysical Journal*, 330, 474
- Pedregosa, F., Varoquaux, G., Gramfort, A., et al. 2011, *Journal of Machine Learning Research*, 12, 2825
- Schmidt, H. U. 1964, *NASA Special Publication*, 50, 107
- Viall, N. M., & Klimchuk, J. A. 2012, *The Astrophysical Journal*, 753, 35
- . 2017, *ApJ*, 842, 108
- Warren, H. P., Winebarger, A. R., Lioello, R., Downs, C., et al. 2016, *ApJ*, 831, 172
- Withbroe, G. L., & Noyes, R. W. 1977, *Annual Review of Astronomy and Astrophysics*, 15, 363
- Young, P. R., Dere, K. P., Landi, E., Zanna, G. D., & Mason, H. E. 2016, *J. Phys. B: At. Mol. Opt. Phys.*, 49, 074009